Simultaneous Perfect Bending and Polarization Rotation of Electromagnetic Wavefront Using Chiral Gradient Metasurfaces

Hamidreza Kazemi,* Mohammad Albooyeh,† and Filippo Capolino‡
Department of Electrical Engineering and Computer Science, University of California, Irvine, California 92697, USA

(Received 10 May 2019; revised manuscript received 28 October 2019; accepted 13 January 2020; published 27 February 2020)

We introduce chiral gradient metasurfaces that allow perfect transmission of the incident wave into a desired direction and simultaneous perfect rotation of the polarization of the refracted wave with respect to the incident one. In the lossless limit, transmission can reach 100% with a single metasurface layer. Besides using gradient polarization densities that provide *bending* of the refracted wave with respect to the incident one, the use of metasurface inclusions that are *chiral* allows the *polarization* of the refracted wave to be rotated. We suggest a possible realization of the proposed device by discretizing the required equivalent-surface polarization densities and synthesizing the chiral discrete polarizabilities with properly sized helical inclusions at each discretization point. By using only a single optically thin layer of chiral inclusions, we are able to deflect a normal incident plane wave to a refracted plane wave at 45° with a 72% power efficiency that is accompanied by a 90° polarization rotation. The proposed concepts and the design method may find practical applications in polarization-rotation devices in microwaves as well as in optics, especially when the incident power is required to be deflected.

DOI: 10.1103/PhysRevApplied.13.024078

I. INTRODUCTION

From the beginning of the twenty-first century, the investigation of metasurfaces, i.e., optically thin layers of arrayed subwavelength inclusions, to shape the wavefronts of electromagnetic waves at will has been dramatically increased compared to that of bulky metamaterials [1–25]. This is because metasurfaces have, in general, smaller losses and easier manufacturing processes compared to bulky engineered metamaterials. Quite recently, by applying the so-called generalized laws of reflection and refraction, specifically designed phase-gradient metasurfaces have achieved about 25% of the transmitted power for the manipulation of transmitted waves [26,27]. Such designs suffered from a lack of degrees of freedom for controlling the polarization of the refracted wave. Subsequent attempts, based on generalized boundary conditions, have accomplished more efficient power operation (about 80%) and have also enabled the manipulation of polarization [28–31]. Simultaneous control of the reflected or transmitted phase and the amplitude is achieved using anisotropic metasurface elements with enough degrees of freedom that lead to both deflection and polarization rotation such as the Y-shaped elements in Ref. [32], yet without devising a robust method that maximizes power transfer.

Most recently, a theoretical scheme for gradient (spatially dispersive) metasurfaces, which offers perfect control of refracted and reflected waves (i.e., 100% power efficiency), has been introduced in the seminal studies in Refs. [3,19,21]. Based on that scheme, metasurface designs for several interesting applications involving wavefront control have been proposed (see, e.g., Refs. [33–40]). However, no work has yet been carried out based on that scheme for the concurrent control of both the direction and polarization of the refracted wavefront. Therefore, it is timely and essential to introduce a realization of gradient metasurfaces that not only deflect the wavefront as desired but also manipulate its polarization at will.

Metasurfaces for both polarization conversion and wavefront manipulation may find a wide range of applications in problems in frequency ranges spanning from microwaves to optics. For instance, metasurface-based polarization rotators are suitable replacements for bulky wave plates (quarter-wavelength, half-wavelength, etc.). Next, metasurface-based wave deflectors are handy candidates to take over the commonly used bulky optical beam splitters that deflect the wavefront of light (45° deflection with 50% power efficiency) in optical systems [9,41,42]. Moreover, polarization-selective metasurfaces are applied for coding the information into different polarization states [43–45]. Furthermore, metasurface-based polarization convertors have been used in microwaves and

*hamidrkazemi87@gmail.com
†mohammad.albooyeh@gmail.com
‡f.capolino@uci.edu

optics for many different applications such as reflector antennas [10,43,46–48], spectral and polarimetric filters [49–51], imaging systems [52,53], and remote sensors [54, 55]. The deflection mechanism can be applied to achieve super-resolution lenses, clocking, and beam steering [32, 56,57] and here it is augmented with polarization control. Furthermore, the proposed method can be generalized to lensing applications in which the polarization is controlled.

Here, we synthesize a planar transmitting metasurface that perfectly deflects the normal (with respect to the metasurface plane) incoming wavefront by 45° and concurrently rotates its polarization by 90°, while we suggest that a similar design procedure can be performed for any arbitrary angle of deflection and any polarization rotation. Our synthesis approach is based on the realization of the desired electric and magnetic equivalent-surface polarization densities, which are connected to the total fields on both sides of the metasurface through the "sheet boundary conditions," as described in Sec. II. We further analyze the metasurface performance for the obtained electric and magnetic polarization densities when they are discretized into five sampling points for each supercell. In Sec. III, we present a physical-realization design that almost satisfies the required equivalent polarization densities that have been obtained in the previous section. The design is composed of five unit cells that form a supercell. Each unit cell consists of four interlaced helices, which fulfills the desired polarization densities when judiciously engineered. The performance of this metasurface design is compared with the ideal case and a power-transmission efficiency of 72% is achieved for a 90° polarization rotation and a 45° wavefront deflection that is much higher than the 25% efficiency reported in the literature for a smaller angle of wavefront deflection (e.g., 30°) using the so-called generalized laws of reflection and refraction (see, e.g., Ref. [58]).

We emphasize that besides being electromagnetically thin, our proposed strategy offers two simultaneous functionalities, i.e., wavefront bending along with polarization rotation of the incoming wavefront, in a single-layer design with a high efficiency. Such a device dramatically reduces the required space by combining the advantages of these two functionalities. Indeed, it can be used in place of two most commonly used kinds of optical apparatus, i.e., a wave plate and a beam splitter, which are bulky and occupy substantial amounts of space. Moreover, our proposal has the advantage of perfect performance (refraction and polarization rotation) when compared to these devices.

II. PROBLEM DESCRIPTION

Let us consider a general metasurface that *perfectly* refracts an incident plane wave with incoming angle θ_i to a plane wave with a desired refraction angle θ_t and converts the incident-field polarization to a favorable one in the refracted field (see Fig. 1).

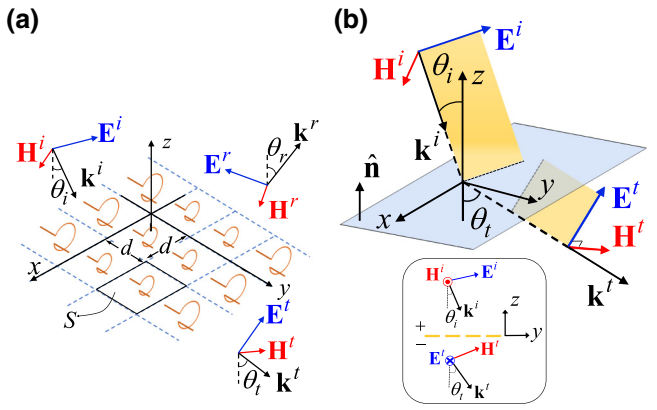

FIG. 1. (a) The general gradient metasurface and depictions of the incident, reflected, and transmitted waves. (b)The incident and refracted waves and polarization of the fields for a reflectionless metasurface.

To elaborate the concepts in a simple manner, let us now make our analysis more specific and consider an incident plane wave with a transverse-magnetic (TM, with respect to z) polarization that is going to be refracted as a transverse-electric (TE) polarized plane wave as shown in the inset of Fig. 1(b). In this example, the polarization of the refracted wave is hence rotated by 90° with respect to that of the incident wave. Next, assuming a time-harmonic wave with time dependence $e^{j\omega t}$ that travels downward, i.e., in the $-z$ direction [see Fig. 1(b)], the electric field vector of the incident wave reads $\mathbf{E}^i = E_0^i \left(\hat{\mathbf{y}} \cos\theta_i e^{-jk_0(\sin\theta_i y - \cos\theta_i z)} + \hat{\mathbf{z}} \sin\theta_i e^{-jk_0(sin\theta_i y - \cos\theta_i z)}\right)$ and that of the refracted wave reads $\mathbf{E}^t = -\hat{\mathbf{x}} E_0^t e^{-jk_0(\sin\theta_t y - \cos\theta_t z) - j\varphi_t}$. Here, $\hat{\mathbf{x}}$, $\hat{\mathbf{y}}$, and $\hat{\mathbf{z}}$ are the unit vectors in Cartesian coordinates, whereas y and z are, accordingly, the position variables. Moreover, k_0 is the free-space wave number and E_0^i and E_0^t are the electric field amplitudes of the incident and refracted waves, respectively. For simplicity, we assume E_0^i and E_0^t to be real valued and φ_t to account for a possible phase shift between the incident and refracted waves upon crossing the metasurface. The tangential electric $\mathbf{E}_t$ and magnetic $\mathbf{H}_t$ fields (the subscript t denotes the tangential component with respect to the metasurface plane) at the boundary of the metasurface, on both the upper and the lower sides, assuming that the metasurface is located on the $z = 0$ plane, read, respectively, as follows:

$$\begin{aligned} \mathbf{E}_{t+} &= \hat{\mathbf{y}} E_0^i \cos\theta_i e^{-jk_0 \sin\theta_i y}, \\ \mathbf{E}_{t-} &= -\hat{\mathbf{x}} E_0^t e^{-jk_0 \sin\theta_t y - j\varphi_t}, \end{aligned} \tag{1}$$

$$\begin{aligned} \hat{\mathbf{n}} \times \mathbf{H}_{t+} &= \hat{\mathbf{y}} \frac{E_0^i}{\eta_0} e^{-jk_0 \sin\theta_i y}, \\ \hat{\mathbf{n}} \times \mathbf{H}_{t-} &= -\hat{\mathbf{x}} \frac{\cos\theta_t}{\eta_0} E_0^t e^{-jk_0 \sin\theta_t y - j\varphi_t}. \end{aligned} \tag{2}$$

Here, the subscripts "$t+$" and "$t-$" refer to the tangential fields at the upper ($z > 0$) and lower ($z < 0$) metasurface boundaries, respectively. Furthermore, $\eta_0 = \sqrt{\mu_0/\epsilon_0}$ is the intrinsic wave impedance of free space and $\hat{\mathbf{n}}$ is the unit vector normal to the metasurface plane in the $+z$ direction [see Fig. 1(b)]. From Eq. (1), the phase of the transmission coefficient reads

$$\Phi_t = k_0 \left(\sin\theta_i - \sin\theta_t\right) y + \varphi_t, \tag{3}$$

which is obviously not uniform over the surface, since $\theta_i \neq \theta_t$ and, indeed, it varies linearly with y. (Other nonlinear variation may be required for other applications, e.g., focusing [32,59].)

In the next step, we write the boundary conditions that connect the jump of tangential fields on both sides of the metasurface to the induced equivalent electric $\mathbf{P}$ (with units of A s m^{-1}) and magnetic $\mathbf{M}$ (with units of V s m^{-1}) *surface* polarization densities satisfying [1,60,61]

$$\mathbf{E}_{t+} - \mathbf{E}_{t-} = j\,\omega \hat{\mathbf{n}} \times \mathbf{M}, \tag{4}$$

$$\hat{\mathbf{n}} \times \mathbf{H}_{t+} - \hat{\mathbf{n}} \times \mathbf{H}_{t-} = j\,\omega \mathbf{P}, \tag{5}$$

where ω is the angular frequency. Therefore, by plugging Eqs. (1), (2), and (3) into Eqs. (4) and (5), the required electric and magnetic equivalent-surface polarization densities for the proposed field manipulation read, respectively, as follows:

$$\mathbf{P} = \frac{E_0^i}{j\,\omega\eta_0} e^{-jk_0 \sin\theta_i y} \left[-\cos\theta_t\, t_{xy} e^{-j\,\Phi_t} \hat{\mathbf{x}} + \hat{\mathbf{y}}\right], \tag{6}$$

$$\mathbf{M} = \frac{E_0^i}{j\,\omega} e^{-jk_0 \sin\theta_i y} \left[\cos\theta_i \hat{\mathbf{x}} - t_{xy} e^{-j\,\Phi_t} \hat{\mathbf{y}}\right]. \tag{7}$$

Here, the TM-to-TE-polarized wave-transmission coefficient $t_{xy} = E_x^t/E_y^i = E_0^t/\left(E_0^i \cos\theta_i\right)$ and by neglecting losses it is approximated as

$$t_{xy} = \frac{1}{\sqrt{\cos\theta_i \cos\theta_t}}, \tag{8}$$

where we consider $E_x^t = E_0^t$ and $E_y^i = E_0^i \cos\theta_i$ (for a proof, see the Appendix). Note that the transmission coefficient here is defined with respect to the transverse component of the electric field in the two half-spaces; thus, t_{xy} can be larger than unity for an oblique incident or transmission angle, without contradicting the power-conservation law.

A. Illustrative example

Let us now consider a specific example in which $\theta_i = 0$ and $\theta_t = \pi/4$ and with each unit cell having the dimensions d along the x axis and D along the y axis, as shown in Fig. 2(a). Figures 2(b) and 2(c) show the required electric and magnetic equivalent polarization densities described by Eqs. (6) and (7) in a unit cell (supercell) for such a metasurface with the mentioned characteristic, i.e., $\theta_i = 0$ and $\theta_t = \pi/4$.

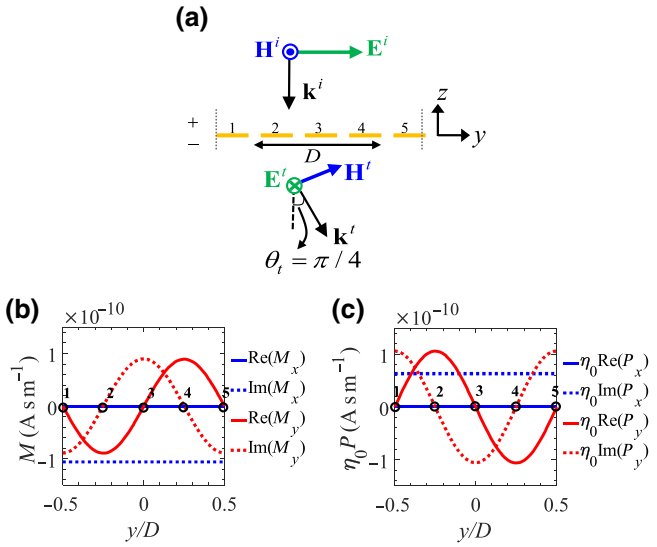

FIG. 2. (a) A schematic of the incident electric field polarized along y (E_y) propagating normally and of the transmitted wave propagating at an angle from the normal direction with a rotated polarization along x (E_x). (b) The desired magnetic and (c) electric polarization densities of a supercell for y-polarized to x-polarized electric field conversion in transmission, where $E_0^i = 1\,\mathrm{V\,m^{-1}}$. The black circles in this figure show the discretization points of the polarization densities on the y axis.

The obtained equivalent surface polarization densities are continuous, uniform in the x direction, and periodic in the y direction (with period D). However, in general, a metasurface is practically composed of discrete elements that mimic such continuous polarization densities. In order to realize a practical design with discrete elements, we sample the desired continuous equivalent magnetic and electric polarization densities given in Figs. 2(b) and 2(c) at a finite number of sampling points in the y direction, within each supercell. In the following example, the magnetic and electric polarization densities are sampled at five equidistant points, $D = 5d$, where impressed magnetic and electric dipole sources are then located in place of the continuous distribution of polarization densities. We plot the simulation results (using the finite-element method implemented in COMSOL MULTIPHYSICS [62]) of the electric field distribution resulting from the discrete sources and the incident plane wave: the y component of the incident electric field and the x component of the refracted field are shown in Fig. 3.

It is clear from the field-distribution maps that the power is perfectly refracted by 45° and rotated by 90° and, moreover, as expected, the energy density of the refracted wave is lower than that of the incident one, since the total power of the refracted wave is set to be equal to the incident

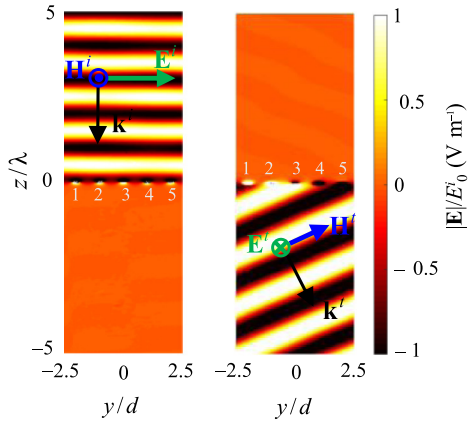

FIG. 3. The normalized electric field distribution (snapshot at a given time) of a perfectly refracting and polarization-rotating metasurface on both sides of the metasurface. The result is based on calculating the scattered field as generated by electric and magnetic point-dipole sources located at five sampling points. The incident field is polarized along y (E_y) and does not experience reflection, i.e., no standing wave is present. The transmitted electric field is polarized along x (E_x) and it is refracted at an oblique angle $\theta_t = 45°$. Total transmission is achieved, i.e., there is no reflection.

power (for more discussion about energy and power densities, see the Appendix). There is no reflection, as can be observed by the lack of any standing wave.

B. Possible physical topologies

The result of the previous section indicates the required polarization densities without any discussion about a feasible realization. In order to understand possible topologies for the realization of a metasurface that acquires the proposed equivalent polarization densities, it is helpful to understand what kinds of scatterers (elements or inclusions) are able to create such polarization densities. Considering inclusion realizations that are well approximated by dipole moments, the electric and magnetic polarization densities so far described are realized by using electric $\mathbf{p}_t = \mathbf{P}S$ and magnetic $\mathbf{m}_t = \mathbf{M}S$ equivalent dipole polarizations per unit cell, where S is the unit-cell area [see Fig. 1(a)]. One practical tool is to study the relation between the fields and the equivalent dipole polarizations per unit cell, i.e., the constitutive relations. Indeed, the tangential components of the equivalent-dipole polarization densities $\mathbf{p}_t$ and $\mathbf{m}_t$ and the tangential incident-field components $\mathbf{E}_t^i$ and $\mathbf{H}_t^i$ are related through the tangential components of the collective polarizabilities $\bar{\bar{\boldsymbol{\alpha}}}_t^{\mathrm{ee}}$, $\bar{\bar{\boldsymbol{\alpha}}}_t^{\mathrm{em}}$, $\bar{\bar{\boldsymbol{\alpha}}}_t^{\mathrm{me}}$, and $\bar{\bar{\boldsymbol{\alpha}}}_t^{\mathrm{mm}}$ of the metasurface unit cells via the constitutive relations [1,63,64]

$$\mathbf{p}_t = \bar{\bar{\boldsymbol{\alpha}}}_t^{\mathrm{ee}} \cdot \mathbf{E}_t^i + \bar{\bar{\boldsymbol{\alpha}}}_t^{\mathrm{em}} \cdot \mathbf{H}_t^i, \tag{9}$$

$$\mathbf{m}_t = \bar{\bar{\boldsymbol{\alpha}}}_t^{\mathrm{me}} \cdot \mathbf{E}_t^i + \bar{\bar{\boldsymbol{\alpha}}}_t^{\mathrm{mm}} \cdot \mathbf{H}_t^i. \tag{10}$$

In the above equations, $\bar{\bar{\boldsymbol{\alpha}}}_t^{\mathrm{ee}}$, $\bar{\bar{\boldsymbol{\alpha}}}_t^{\mathrm{em}}$, $\bar{\bar{\boldsymbol{\alpha}}}_t^{\mathrm{me}}$, and $\bar{\bar{\boldsymbol{\alpha}}}_t^{\mathrm{mm}}$ are the collective electric, magnetoelectric, electromagnetic, and magnetic polarizability dyadics in the metasurface plane, relating the incident field to the electric and magnetic dipoles. The word *collective* means that the polarizability also accounts for the coupling with all the dipoles in the other unit cells of the array [1,63,65]. Each polarization dyad has four components α_{ij}, where $ij = xx, xy, yx,$ or yy in Cartesian coordinates, i.e., in terms of matrix representation, they are given by

$$\bar{\bar{\alpha}}_t = \begin{bmatrix} \alpha_{xx} & \alpha_{xy} \\ \alpha_{yx} & \alpha_{yy} \end{bmatrix}. \tag{11}$$

Note that in the general case, the polarizability dyadics have nine components; however, for our analysis it is enough to consider only the tangential components (for a more elaborated discussion, see Refs. [12,60]). Next, by substituting the fields from Eqs. (1) and (2) into Eqs. (9) and (10), the equivalent-dipole polarizations in terms of the polarizability components and the incident field read

$$\mathbf{p}_t = \left[\hat{\mathbf{x}}\left(\alpha_{xy}^{\mathrm{ee}}\cos\theta_i + \frac{\alpha_{xx}^{\mathrm{em}}}{\eta_0}\right) + \hat{\mathbf{y}}\left(\alpha_{yy}^{\mathrm{ee}}\cos\theta_i + \frac{\alpha_{yx}^{\mathrm{em}}}{\eta_0}\right)\right] E_0^i e^{-jk_0 \sin\theta_i y}, \tag{12}$$

$$\mathbf{m}_t = \left[\hat{\mathbf{x}}\left(\alpha_{xy}^{\mathrm{me}}\cos\theta_i + \frac{\alpha_{xx}^{\mathrm{mm}}}{\eta_0}\right) + \hat{\mathbf{y}}\left(\alpha_{yy}^{\mathrm{me}}\cos\theta_i + \frac{\alpha_{yx}^{\mathrm{mm}}}{\eta_0}\right)\right] E_0^i e^{-jk_0 \sin\theta_i y}. \tag{13}$$

Based on the above equations, there is obviously not a unique scatterer's topology to deliver the desired performance, since the above are four scalar complex-value equations with eight complex-value unknown polarizability components (four in each polarizability dyad; however, the selected polarizations in this particular case imply that only eight dyad entrees need to be determined). Nevertheless, among all the possible solutions, both the electric and the magnetic polarizations must be simultaneously nonzero, which limits the number of possible solutions. Moreover, in the following we suppress the cross-components of the polarizabilities (i.e., $\alpha_{xy}^{\mathrm{ee}} = \alpha_{yx}^{\mathrm{em}} = \alpha_{xy}^{\mathrm{me}} = \alpha_{yx}^{\mathrm{mm}} = 0$) to narrow down the possible sets of topologies. As a result, the remaining polarizability components imply that the metasurface constitutive inclusions must be chiral, since we require that $\alpha_{xx}^{\mathrm{em}} = -\alpha_{xx}^{\mathrm{me}}, \neq 0$ or $\alpha_{yy}^{\mathrm{em}} = -\alpha_{yy}^{\mathrm{me}}, \neq 0$, for reciprocal lossy and lossless inclusions. By using Eqs. (6) and (7) in Eqs. (12) and (13), the collective polarizabilities for the proposed chiral

metasurface are

$$\begin{aligned}\alpha_{xx}^{\mathrm{em}} &= -\frac{S}{j\omega}\cos\theta_t t_{xy} e^{-j\Phi_t},\\ \alpha_{yy}^{\mathrm{ee}} &= \frac{S}{j\omega}\frac{1}{\eta_0\cos\theta_i},\\ \alpha_{xx}^{\mathrm{mm}} &= \frac{S}{j\omega}\eta_0\cos\theta_i,\\ \alpha_{yy}^{\mathrm{me}} &= -\frac{S}{j\omega}\frac{t_{xy}}{\cos\theta_i}e^{-j\Phi_t}.\end{aligned} \tag{14}$$

In the next section, we propose a physical element that exhibits these polarizability components, i.e., the desired equivalent-dipole polarizations and, hence, the required equivalent-surface polarization densities under the given illumination.

III. PHYSICAL REALIZATION

In this section, we first propose a unit-cell design that perfectly rotates the polarization of the incoming wave at a normal incidence by 90°. Hence, in the first step, we do not generate plane-wave deflection. This latter feature will be realized as a second step by applying the designed unit cell of this first step and constructing a gradient metasurface, to achieve a perfect deflection of a normal incident wave to a 45° refracted wave.

A. Unit-cell design for polarization rotation

It is well known that, if excited properly, a helical-wire particle may acquire the polarizabilities described by Eqs. (14) (see Refs. [66,67]). Here, we use helices with axes belonging to the transverse metasurface plane, since we are interested in inducing TE and TM dipoles. To optimize the performance of a chiral particle, Semchenko *et al.* introduced optimal helices in Ref. [68] (i.e., helices with equal electric, magnetic, and magneto-electric polarizabilities, which means that $|\alpha^{\mathrm{em}}| = |\eta_0\alpha^{\mathrm{ee}}| = |\alpha^{\mathrm{mm}}/\eta_0|$), which we use here as a part of the design. Such an inclusion provides a maximum cross-polarized transmission when implemented as the building block of a metasurface. The basic building block of a metasurface unit cell is the single optimal helix shown in Fig. 4(a). In particular, we consider a single helix made of one turn. The structural parameters, i.e., the helix radius $r = 14$ mm, helix pitch $p = 16.3$ mm, and unit-cell period $d = 56.5$ mm, of the designed helices are illustrated in Fig. 4(a). Moreover, the helix axis is oriented along the $\varphi = -45°$ direction, as shown in Fig. 4(a), and the metal is assumed to be a perfect conductor with radius $r_w = 0.1$ mm.

The copolarized (i.e., along the same direction as the incident electric field) and cross-polarized (i.e., orthogonal to the direction of the incident electric field) field components that define the reflection and transmission

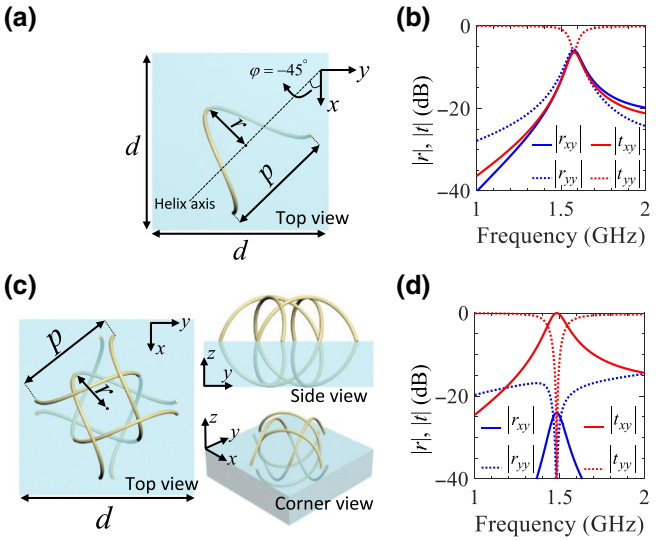

FIG. 4. (a) The top view of a single-helix unit cell with subwavelength dimensions. (b) The reflection and transmission coefficients of y- and x-polarized waves for the infinite planar periodic array of unit cells in (a). (c) The geometry and different view angles of the designed particle composed of four interlaced helices as in (a). (d) The reflection and transmission coefficients of the y- and x-polarized waves for an infinite planar periodic array of unit cells shown in (c).

coefficients of a metasurface composed of the unit cell with a single helix in Fig. 4(a) are shown in Fig. 4(b). The subscripts yy and xy refer to the co- and cross-polarization components, respectively, in a linear-polarization basis, with the incident electric polarization oriented along the y direction. As stated earlier, in the first step we seek a metasurface that is able to perfectly refract the normal incident plane with 90° rotation of the polarization with respect to that of the incident wave, without generating any angular deflection, i.e., the transmitted wave is propagating along the normal direction (the z direction). In terms of reflection and/or transmission coefficients, this means that

$$\begin{aligned}t_{xy} &= 1,\\ t_{yy} &= r_{xy} = r_{yy} = 0,\end{aligned} \tag{15}$$

As is clear from Fig. 4(b), although such a design provides a maximum possible cross-polarized transmission with an individual single-turn helix in each unit cell, it does not grant perfect transmission of all the incident power to the desired rotated polarization (note that $|t_{xy}| \neq 1$). Indeed, since the magnitudes of all the reflection and transmission coefficients in Fig. 4(b) are approximately equal to each other at the desired frequency (at approximately 1.5 GHz), the incident power is divided approximately evenly between all of the components of the reflection and transmission spectra at this frequency; hence Eqs. (15) are not satisfied. However, when we increase the number of

helices in a unit cell with a proper orientation, as mentioned in Ref. [69], i.e., four helices that are rotated by 90° around the z axis with respect to each other, then, remarkably, a reflectionless surface can be achieved. Nevertheless, the design in Ref. [69] has a unit-cell size that exceeds the operational wavelength; hence it is not a practical design for metasurfaces with incident (refracted) angles rather than normal incidence (refraction). Therefore, here we use four interlaced helices in a single unit cell to be sure that the unit cell size is subwavelength, a feature that is useful for the implementation of a gradient metasurface that generates a transmitted wave with a 45° deflection, discussed in the next subsection. Figure 4(c) shows the configuration of the four interlaced helices in each unit cell that provide a fully transmittive (i.e., reflectionless) metasurface that perfectly rotates the polarization of the normal incoming wave by 90°. This unit cell is composed of four identical cocentered helices, in which the axes lie on the x-y plane and are rotated by 90° around the z axis. The orientation, spatial position, and structural parameters of the designed helices are illustrated in Fig. 4(c), where the structural parameters for each helix are the same as those for the single-helix unit cell in Fig. 4(a). Note that the helices in this design have no electrical connection. A periodic array composed of an infinite number of such chiral unit cells with $d = \sqrt{2}\lambda/5$, where λ is the wavelength of the plane wave, shows a perfect y-to-x polarization rotation at the frequency of 1.5 GHz, as shown in Fig. 4(d), since the reflection and transmission coefficients of such a metasurface satisfy Eqs. (15). Deduced from this figure, the incident wave with its electric field polarization along y is perfectly transmitted into a transmitted wave with electric field polarization along x, propagating in the lower half-space. It is obvious from this figure that at 1.5 GHz, both the x- and y-polarized reflected waves are negligible.

B. Supercell design for wavefront deflection

In this section, we use a modulation of the metasurface parameters that, based on the generalized Snell's law, leads to the transmission phase in Eq. (3). Following this approach, the shape of the wavefront refracted by the array relies on the gradual increase of the transmission phase along the supercell constitutive elements [19,26,32,59,70]. Such a gradual phase increase along the metasurface is provided by suitably engineering each constitutive inclusion in the so-called "supercell" and since the phase variation is along the y direction, the supercell is defined by modulating a few unit cells along the y direction, while it has the dimension of a single unit cell in the x direction. According to the example in the previous section and Eq. (3), considering normal incidence, a required 45° transmission-angle deflection, and assuming that $\varphi_t = 0$ without loss of generality, the transmission phase will increase linearly in the y direction as

$$\Phi_t(y) = -\frac{k_0}{\sqrt{2}}y. \tag{16}$$

This required transmission phase is a continuous function of position y along the surface. However, as discussed before, for a practical realization, the continuous distribution of the electric and magnetic polarization densities is realized in a discretized fashion, i.e., by a finite number of electric and magnetic induced dipole moments in each supercell. The desired phase distribution across the metasurface is obtained by meticulously optimizing the dimensions of the four interlaced helices in a few unit cells that make up the supercell. In the present realization, the supercell is divided into five unit cells as shown in the image at the bottom of Table I, which shows the optimized dimensions of the helices in each of the five unit cells. The required transmission phases at the locations of the five different unit cells are obtained from Eq. (16), where $y = \pm nd$, $n = 0, 1, 2$. Note that all the four helices in each individual unit cell are identical.

Therefore, the metasurface is made of an array of supercells with dimensions d along the x direction and $5d$ along the y direction. The design of the supercell elements is done as follows. First, we design five distinct metasurfaces, each one being made of a periodic array of each of the unit cells in Table I, with period d in both the x and y directions. The full-wave simulation based on the finite-element method is based on periodic boundary conditions. Therefore, a single unit cell of dimensions $d \times d$ is simulated for normal plane-wave incidence and the transmitted phase is evaluated for each type of these five metasurfaces. For each metasurface, the dimensions are optimized to provide a perfect cross-polarized transmittance (this is possible based on the results of the previous subsection) and the transmission phase given in Table I. The resulting magnitude and phase of the y- to x-polarized wave-transmission coefficient t_{xy} is depicted in Fig. 5 for the five different metasurfaces, each one based on a different inclusion's dimensions as given in Table I.

TABLE I. The helix radius, helix pitch, and handedness of the five different inclusions (the helices are identical in each cluster). In the table, R and L denote the right- and left-handed helices.

	No. 1	No. 2	No. 3	No. 4	No. 5
r (mm)	13.23	13.76	14.24	13.30	14.24
p (mm)	17.13	17.8	18.43	17.22	18.43
Handedness	L	L	L	R	R
Φ_t (degrees)	120	80	41	−73	−140

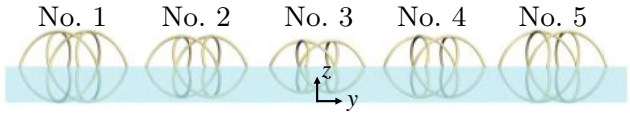

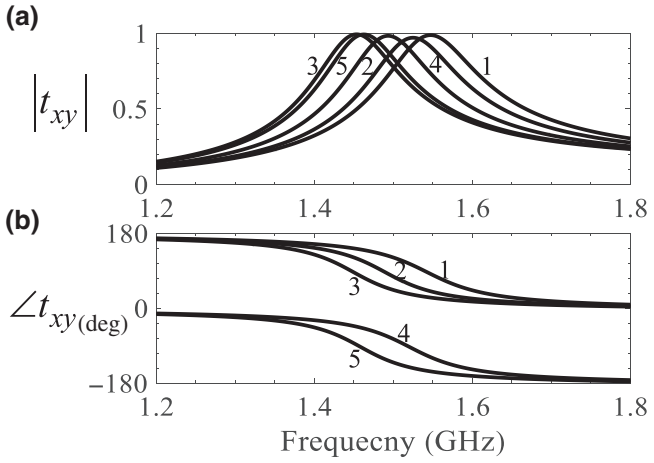

FIG. 5. The magnitude and phase of the t_{xy} transmission coefficient for the five different metasurfaces, each one based on one unit-cell design in Table I: (a) the magnitude and (b) the phase of the cross-polarization transmission coefficient t_{xy}. When it reaches 1, all the power is transmitted with a polarization rotation of 90°, as discussed in Sec. A. The phase-gradient metasurface is then made with a supercell with dimensions $d \times 5d$, by arranging sequentially the five properly designed unit cells.

Next, the gradient metasurface to provide an angular deflection of 45° is made of a periodic arrangement of supercells with dimensions d along the x direction and $5d$ along the$y$ direction. As a result, the designed metasurface has a desired periodic phase distribution along the y direction [see Eq. (16)] and a uniform phase distribution along the x direction. The field distribution in the proximity of the engineered gradient metasurface, excited with a normally incident plane wave polarized along the y direction, is illustrated in Fig. 6(a), where the field distribution is calculated with a full-wave simulation based on the finite-element method. The distributions of the y polarization (left) and the x polarization (right) of the electric field are plotted in Fig. 6(a) at a frequency of $f = 1.5$ GHz. In this simulation based on the finite-element method, periodic boundaries are chosen to mimic the infinite extension of the metasurface along both the x and y directions, i.e., modeling a periodic supercell of dimensions $d \times 5d$. In this combined design, we account for losses, i.e., the helices are made of copper and are embedded in a foam (FR 3703 from General Plastics) with a dielectric constant of 1.06 and a loss tangent of 0.0004, as in Fig. 4. As is clear from Fig. 6, the gradient metasurface rotates the polarization of the incident wave by 90° and refracts it into $\theta_t = 45°$. The result in Fig. 6(a) does not show the perfect polarization rotation and deflection, as does the ideal case in Fig. 3, because in the actual design of the gradient metasurface we use the concept of local periodicity in designing the five unit cells of the supercell, which is a standard approximation in metasurface and reflectarray design [32,71] but which is not fully accurate. As a

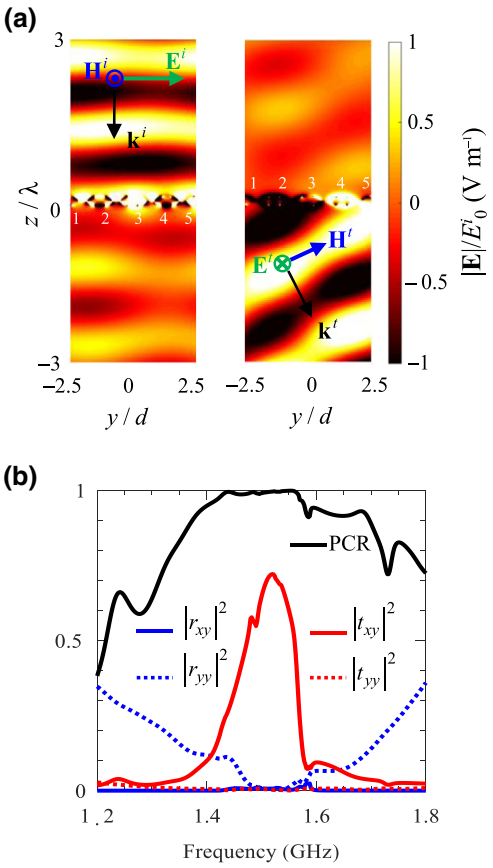

FIG. 6. (a) The full-wave simulation for the field distribution resulting from normal plane-wave incidence from the top on the designed metasurface, the supercell of which is made of five unit cells with parameters given in Table I: left, the y polarization of the electric field, showing mainly the incident field; right, the x polarization of the electric field, showing mainly the deflected transmitted field. It is clear that besides deflecting the wavefront, the metasurface also rotates the polarization by 90° degrees. (b) A plot of the PCR, the y- to x-polarized power-reflection and power-transmission coefficients versus the frequency, showing an almost 100% polarization rotation, and the y- to x-polarized power-transmission coefficient (i.e., the cross-polarized power transmission), showing a 72% power-transmission efficiency. Metal and dielectric losses are accounted for in this simulation.

measure of the metasurface performance, we define the polarization conversion ratio (PCR) in transmission as

$$e_{\mathrm{PCR}} = \frac{|t_{xy}|^2}{|t_{yy}|^2 + |t_{xy}|^2}, \tag{17}$$

where $|t_{xy}|$ and $|t_{yy}|$ are the magnitude of the y- to x-polarized (cross-polarization component) and y- to y-polarized (co-polarization component) transmission coefficients, respectively. Figure 6(b) shows the PCR versus the frequency, as well as the y- to x-polarized reflectance and transmittance of a y-polarized incident wave. As is obvious from this figure, we obtain a perfect (100%) polarization

conversion and 72% power transmission into the deflected wave with the engineered metasurface. The authors believe that the proposed design is a unique metasurface that provides simultaneous deflection and polarization rotation of incoming wavefront with such high efficiency.

IV. CONCLUSION

In the framework of gradient metasurfaces, we show that, in principle, using chirality, it is possible to obtain perfect polarization rotation of the electromagnetic wavefront with concurrent full transmission into a desired deflected direction. The chirality characteristic of a metasurface serves for polarization rotation of the transmitted plane wave with respect to the incident one, whereas the gradient property (i.e., the spatial dispersion) of the metasurface allows the wavefront deflection. Furthermore, we demonstrate a possible physical realization of the proposed device by engineering a metasurface with proper unit-cell inclusions that realizes the aforementioned combined functionalities. Our full-wave simulation results demonstrate a high transmission power efficiency of 72% at a deflection angle of 45° by using only one single layer of inclusions (i.e., a single metasurface), which is accompanied by a perfect 90° polarization rotation. Despite the fact that the results are shown for a specific illustrative case, the method outlined in this paper is very general and can be used for conceiving metasurfaces that deflect wavefronts at any angle with arbitrary polarization conversion and with (in theory) perfect transmittance.

In short, in a single metasurface, we combine two interesting functionalities, i.e., a wave refraction at a given angle and a polarization rotation, with very high efficiency and subwavelength thickness, by using chiral-metasurface inclusions.

ACKNOWLEDGMENTS

We would like to thank the Dassault Systèmes Simulia Corporation for providing the CST STUDIO SUITE that was instrumental in this study. We also acknowledge support from the W. M. Keck Foundation, USA.

APPENDIX: ENERGY DENSITIES OF THE INCIDENT AND REFRACTED WAVES, POWER BALANCE RELATION, AND TRANSMISSION COEFFICIENT FOR PERFECT POWER TRANSMISSION AND POLARIZATION CONVERSION

The characteristic of the proposed fully transmissive metasurface is such that the wave passes through it without changing its total time-averaged power (when the metasurface is lossless) and the metasurface changes the polarization and the direction of the transmitted wavefront with respect to the incident one. Therefore, the total incident and refracted powers crossing the metasurface along the ray tube in Fig. 7 are equal. Under such conditions, the total time-averaged incident and transmitted field energy densities are required to satisfy

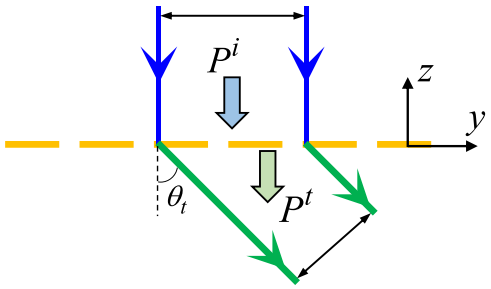

FIG. 7. A schematic of the power flow for a propagating wave when passing through the deflecting metasurface. The metasurface is passive and changes the polarization and the direction of the transmitted wavefront with respect to the incident one.

$$\frac{\mathcal{E}^i}{\mathcal{E}^t} = \frac{\cos\theta_t}{\cos\theta_i}. \tag{A1}$$

Therefore, in this scenario, since the total time-averaged incident and transmitted energy densities, $\mathcal{E}^i$ and $\mathcal{E}^t$, are different, the wave intensity changes when passing through the fully transmissive metasurface. This can also be described in the following manner, by observing the power crossing a plane with constant z, right above and below the metasurface. Of course, such powers are equal to each other when considering a lossless metasurface, which implies the conservation of the normal component of the Poynting vector from above to below the metasurface, i.e.,

$$\frac{1}{2}\mathrm{Re}\left(\mathbf{E}_{t+}\times\mathbf{H}^*_{t+}\right) = \frac{1}{2}\mathrm{Re}\left(\mathbf{E}_{t-}\times\mathbf{H}^*_{t-}\right). \tag{A2}$$

Substituting the fields described in Eqs. (1) and (2) into Eq. (A2) leads to

$$\frac{E_y^{i\,2}}{\cos\theta_i} = \cos\theta_t E_x^{t\,2}, \tag{A3}$$

where $E_y^i = E_0^i\cos\theta_i$ and $E_x^t = E_0^t$, and then

$$t_{xy} = \frac{1}{\sqrt{\cos\theta_i\cos\theta_t}}, \tag{A4}$$

for a reflectionless surface. Thus, for normal incidence, $t_{xy} = 1/\sqrt{\cos\theta_t}$, which is larger than unity for an oblique transmission angle, without contradicting the power-conservation law.

[1] M. Albooyeh, S. Tretyakov, and C. Simovski, Electromagnetic characterization of bianisotropic metasurfaces on refractive substrates: General theoretical framework, Ann. Phys. **528**, 721 (2016).

[2] K. Achouri, M. A. Salem, and C. Caloz, General metasurface synthesis based on susceptibility tensors, IEEE Trans. Antennas Propag. **63**, 2977 (2015).

[3] V. S. Asadchy, M. Albooyeh, S. N. Tcvetkova, A. Diaz-Rubio, Y. Ra'di, and S. A. Tretyakov, Perfect control of reflection and refraction using spatially dispersive metasurfaces, Phys. Rev. B **94**, 075142 (2016).

[4] H. T. Chen, A. J. Taylor, and N. Yu, A review of metasurfaces: Physics and applications, Rep. Progr. Phys. **79**, 076401 (2016).

[5] Y. Cheng, Y. Nie, X. Wang, and R. Gong, An ultrathin transparent metamaterial polarization transformer based on a twist-split-ring resonator, Appl. Phys. A **111**, 209 (2013).

[6] I. Faniayeu, S. Khakhomov, I. Semchenko, and V. Mizeikis, Highly transparent twist polarizer metasurface, Appl. Phys. Lett. **111**, 111108 (2017).

[7] D. L. Markovich, A. Andryieuski, M. Zalkovskij, R. Malureanu, and A. V. Lavrinenko, Metamaterial polarization converter analysis: Limits of performance, Appl. Phys. B **112**, 143 (2013).

[8] C. Menzel, C. Helgert, C. Rockstuhl, E.-B. Kley, A. Tunnermann, T. Pertsch, and F. Lederer, Asymmetric Transmission of Linearly Polarized Light at Optical Metamaterials, Phys. Rev. Lett. **104**, 253902 (2010).

[9] C. Pfeiffer and A. Grbic, Bianisotropic Metasurfaces for Optimal Polarization Control: Analysis and Synthesis, Phys. Rev. Appl. **2**, 044011 (2014).

[10] C. Pfeiffer, C. Zhang, V. Ray, L. J. Guo, and A. Grbic, Polarization rotation with ultra-thin bianisotropic metasurfaces, Optica **3**, 427 (2016).

[11] M. Safari, A. Abdolali, H. Kazemi, M. Albooyeh, M. Veysi, and F. Capolino, in *2017 IEEE International Symposium on Antennas and Propagation USNC/URSI National Radio Science Meeting* (San Diego, CA, USA, 2017), p. 1499.

[12] M. Albooyeh, H. Kazemi, F. Capolino, D. H. Kwon, and S. A. Tretyakov, in *2017 IEEE International Symposium on Antennas and Propagation USNC/URSI National Radio Science Meeting* (San Diego, CA, USA, 2017), p. 1707.

[13] J. Vehmas, Y. Ra'di, A. O. Karilainen, and S. A. Tretyakov, Eliminating electromagnetic scattering from small particles, IEEE Trans. Antennas Propag. **61**, 3747 (2013).

[14] Q. Zheng, C. Guo, H. Li, and J. Ding, Wideband and high efficiency reflective polarization rotator based on metasurface, J. Electromagnetic Waves Appl. **32**, 265 (2018).

[15] Z. Zhu, H. Liu, Z. Jiang, T. Lv, C. Guan, and J. Shi, Manipulating broadband polarization conversion in metamaterials, J. Appl. Phys. **122**, 215101 (2017).

[16] F. Capolino, A. Vallecchi, and M. Albani, Equivalent transmission line model with a lumped X-circuit for a metalayer made of pairs of planar conductors, IEEE Trans. Antennas Propag. **61**, 852 (2013).

[17] S. B. Glybovski, S. A. Tretyakov, P. A. Belov, Y. S. Kivshar, and C. R. Simovski, Metasurfaces: From microwaves to visible, Phys. Rep. **634**, 1 (2016).

[18] S. A. Tretyakov, Metasurfaces for general transformations of electromagnetic fields, Philos. Trans. R. Soc. London A: Math., Phys. Eng. Sci. **373**, 2049 (2015).

[19] J. PS. Wong, A. Epstein, and G. V. Eleftheriades, Reflectionless wide-angle refracting metasurfaces, IEEE Antennas Wirel. Propag. Lett. **15**, 1293 (2015).

[20] H. Kazemi, M. Albooyeh, and F. Capolino, in *2019 URSI International Symposium on Electromagnetic Theory (EMTS)* (San Diego, CA, USA, 2019), p. 1.

[21] N. Mohammadi Estakhri and A. Alù, Wave-Front Transformation with Gradient Metasurfaces, Phys. Rev. X **6**, 041008 (2016).

[22] R. Alaee, M. Albooyeh, S. Tretyakov, and C. Rockstuhl, Phase-change material-based nanoantennas with tunable radiation patterns, Opt. Lett. **41**, 4099 (2016).

[23] M. Albooyeh, R. Alaee, C. Rockstuhl, and C. Simovski, Revisiting substrate-induced bianisotropy in metasurfaces, Phys. Rev. B **91**, 195304 (2015).

[24] Y. Guo, M. Xiao, and S. Fan, Topologically Protected Complete Polarization Conversion, Phys. Rev. Lett. **119**, 167401 (2017).

[25] M. Rajaei, J. Zeng, M. Albooyeh, M. Kamandi, M. Hanifeh, F. Capolino, and H. K. Wickramasinghe, Giant circular dichroism at visible frequencies enabled by plasmonic ramp-shaped nanostructures, ACS Photonics, **6**, 924 (2019).

[26] N. Yu, P. Genevet, M. A. Kats, F. Aieta, J.-P. Tetienne, F. Capasso, and Z. Gaburro, Light propagation with phase discontinuities: Generalized laws of reflection and refraction, Science **334**, 333 (2011).

[27] M. I. Shalaev, J. Sun, A. Tsukernik, A. Pandey, K. Nikolskiy, and N. M. Litchinitser, High-efficiency all-dielectric metasurfaces for ultracompact beam manipulation in transmission mode, Nano. Lett. **15**, 6261 (2015).

[28] F. Monticone, N. M. Estakhri, and A. Alù, Full Control of Nanoscale Optical Transmission with a Composite Metascreen, Phys. Rev. Lett. **110**, 203903 (2013).

[29] C. Pfeiffer and A. Grbic, Millimeter-wave transmitarrays for wavefront and polarization control, IEEE Trans. Microw. Theory. Tech. **61**, 4407 (2013).

[30] M. Kim and G. V. Eleftheriades, Design and demonstration of impedance-matched dual-band chiral metasurfaces, Sci. Rep. **8**, 3449 (2018).

[31] A. Ranjbar and A. Grbic, Broadband, Multiband, and Multifunctional All-Dielectric Metasurfaces, Phys. Rev. Appl. **11**, 054066 (2019).

[32] M. Veysi, C. Guclu, O. Boyraz, and F. Capolino, Thin anisotropic metasurfaces for simultaneous light focusing and polarization manipulation, JOSA B **32**, 318 (2015).

[33] A. A. Elsakka, V. S. Asadchy, I. A. Faniayeu, S. N. Tcvetkova, and S. A. Tretyakov, Multifunctional cascaded metamaterials: Integrated transmitarrays, IEEE Trans. Antennas Propag. **64**, 4266 (2016).

[34] M. Chen, E. Abdo-Sanchez, A. Epstein, and G. V. Eleftheriades, in *2017 XXXIInd General Assembly and Scientific Symposium of the International Union of Radio Science (URSI GASS)* (Montreal, QC, Canada, 2017), p. 1.

[35] V. S. Asadchy, A. Díaz-Rubio, S. N. Tcvetkova, D.-H. Kwon, A. Elsakka, M. Albooyeh, and S. A. Tretyakov,

Flat Engineered Multichannel Reflectors, Phys. Rev. X **7**, 031046 (2017).
[36] N. K. Emani, E. Khaidarov, R. Paniagua-Dominguez, Y. H. Fu, V. Valuckas, S. Lu, X. Zhang, S. T. Tan, H. V. Demir, and A. I. Kuznetsov, High-efficiency and low-loss gallium nitride dielectric metasurfaces for nanophotonics at visible wavelengths, Appl. Phys. Lett. **111**, 221101 (2017).
[37] Y. Radi, D. L. Sounas, and A. Alù, Metagratings: Beyond the Limits of Graded Metasurfaces for Wave Front Control, Phys. Rev. Lett. **119**, 067404 (2017).
[38] A. M. H. Wong, P. Christian, and G. V. Eleftheriades, Binary Huygens' metasurfaces: Experimental demonstration of simple and efficient near-grazing retroreflectors for TE and TM polarizations, IEEE Trans. Antennas Propag. **66**, 2892 (2018).
[39] O. Rabinovich and A. Epstein, Analytical design of printed-circuit-board (PCB) metagratings for perfect anomalous reflection, IEEE Trans. Antennas Propag. **66**, 4086 (2018).
[40] O. Rabinovich and A. Epstein, Arbitrary diffraction engineering with multilayered multielement metagratings, arXiv preprint arXiv:1905.02376 (2019).
[41] N. Yu, F. Aieta, P. Genevet, M. A. Kats, Z. Gaburro, and F. Capasso, A broadband, background-free quarter-wave plate based on plasmonic metasurfaces, Nano Lett. **12**, 6328 (2012).
[42] C. Wu, N. Arju, G. Kelp, J. A. Fan, J. Dominguez, E. Gonzales, E. Tutuc, I. Brener, and G. Shvets, Spectrally selective chiral silicon metasurfaces based on infrared Fano resonances, Nat. Commun. **5**, 3892 (2014).
[43] M. Selvanayagam and G. V. Eleftheriades, Design and measurement of tensor impedance transmitarrays for chiral polarization control, IEEE Trans. Microw. Theory Tech. **64**, 414 (2016).
[44] J. Li, P. Yu, H. Cheng, W. Liu, Z. Li, B. Xie, S. Chen, and J. Tian, Optical polarization encoding using graphene-loaded plasmonic metasurfaces, Adv. Opt. Mater. **4**, 91 (2016).
[45] M. Kim and G. V. Eleftheriades, Highly efficient all-dielectric optical tensor impedance metasurfaces for chiral polarization control, Opt. Lett. **41**, 4831 (2016).
[46] Y. Jia, Y. Liu, Y. J. Guo, K. Li, and S. X. Gong, Broadband polarization rotation reflective surfaces and their applications to RCS reduction, IEEE Trans. Antennas Propag. **64**, 179 (2016).
[47] M. Farmahini-Farahani and H. Mosallaei, Birefringent reflectarray metasurface for beam engineering in infrared, Opt. Lett. **38**, 462 (2013).
[48] N. Amitay and A. Saleh, Broad-band wide-angle quasi-optical polarization rotators, IEEE Trans. Antennas Propag. **31**, 73 (1983).
[49] J. H. Shi, H. F. Ma, W. X. Jiang, and T. J. Cui, Multiband stereometamaterial-based polarization spectral filter, Phys. Rev. B **86**, 035103 (2012).
[50] V. Gruev, J. Van der Spiegel, and N. Engheta, Sensor and polarimetric filters for real-time extraction of polarimetric information at the focal plane, U.S. Patent 7, 582, 857, (2009).
[51] A. Bodkin and J. T. Daly, Optical systems and methods employing a polarimetric optical filter, U.S. Patent 9, 347, 832, (2016).
[52] R.-H. Fan, Y. Zhou, X.-P. Ren, R.-W. Peng, S.-C. Jiang, D.-H. Xu, X. Xiong, X.-R. Huang, and M. Wang, Freely tunable broadband polarization rotator for terahertz waves, Adv. Mater. **27**, 1201 (2015).
[53] C. Dietlein, A. Luukanen, Z. Popovi, and E. Grossman, A *W*-band polarization converter and isolator, IEEE Trans. Antennas Propag. **55**, 1804 (2007).
[54] R. Dickie, R. Cahill, V. Fusco, H. S Gamble, and N. Mitchell, THz frequency selective surface filters for earth observation remote sensing instruments, IEEE Trans. Terahertz. Sci. Technol. **1**, 450 (2011).
[55] M. Euler, V. Fusco, R. Cahill, and R. Dickie, 325 GHz single layer sub-millimeter wave FSS based split slot ring linear to circular polarization convertor, IEEE Trans. Antennas Propag. **58**, 2457 (2010).
[56] N. M. Mohammadi Estakhri and A. Alù, Ultra-thin unidirectional carpet cloak and wavefront reconstruction with graded metasurfaces, IEEE Antennas Wirel. Propag. Lett. **13**, 1775 (2014).
[57] C. Huang, W. Pan, X. Ma, B. Zhao, J. Cui, and X. Luo, Using reconfigurable transmitarray to achieve beam-steering and polarization manipulation applications, IEEE Trans. Antennas Propag. **63**, 4801 (2015).
[58] F. Aieta, P. Genevet, N. Yu, M. A. Kats, Z. Gaburro, and F. Capasso, Out-of-plane reflection and refraction of light by anisotropic optical antenna metasurfaces with phase discontinuities, Nano Lett. **12**, 1702 (2012).
[59] M. Khorasaninejad, F. Aieta, P. Kanhaiya, M. A. Kats, P. Genevet, D. Rousso, and F. Capasso, Achromatic metasurface lens at telecommunication wavelengths, Nano Lett. **15**, 5358 (2015).
[60] M. Albooyeh, D.-H. Kwon, F. Capolino, and S. A. Tretyakov, Equivalent realizations of reciprocal metasurfaces: Role of tangential and normal polarization, Phys. Rev. B **95**, 115435 (2017).
[61] M. Safari, H. Kazemi, A. Abdolali, M. Albooyeh, and F. Capolino, Illusion mechanisms with cylindrical metasurfaces: A general synthesis approach, Phys. Rev. B **100**, 165418 (2019).
[62] COMSOL MULTIPHYSICS reference manual, version 5.3, Comsol, Inc., https://www.comsol.com.
[63] A. Serdiukov, I. Semchenko, S. Tertyakov, and A. Sihvola, *Electromagnetics of Bi-Anisotropic Materials-Theory and Application* (Gordon and Breach Science Publishers, 2001), Vol. 11.
[64] M. Hanifeh and F. Capolino, Helicity density enhancement in a planar array of achiral high-density dielectric nanoparticles, Eprint ArXiv1905.03387 (2019).
[65] M. Albooyeh, V. Asadchy, J. Zeng, H. Kazemi, and F. Capolino, in *2019 URSI International Symposium on Electromagnetic Theory (EMTS)* (2019), p. 1.
[66] S. A. Tretyakov, F. Mariotte, C. R. Simovski, T. G. Kharina, and J. P. Heliot, Analytical antenna model for chiral scatterers: Comparison with numerical and experimental data, IEEE Trans. Antennas Propag. **44**, 1006 (1996).
[67] I. Fernandez-Corbaton, C. Rockstuhl, P. Ziemke, P. Gumbsch, A. Albiez, R. Schwaiger, T. Frenzel, M. Kadic, and M. Wegener, New twists of 3D chiral metamaterials, Adv. Mater. **31**, 1807742 (2019).

[68] I. V. Semchenko, S. A. Khakhomov, and A. L. Samofalov, Optimal helix shape: Equality of dielectric, magnetic, and chiral susceptibilities, Russ. Phys. J. **52**, 472 (2009).

[69] V. S. Asadchy, I. A. Faniayeu, Y. Ra'di, S. A. Khakhomov, I. V. Semchenko, and S. A. Tretyakov, Broadband Reflectionless Metasheets: Frequency-Selective Transmission and Perfect Absorption, Phys. Rev. X **5**, 031005 (2015).

[70] N. Mohammadi Estakhri and A. Alu, Recent progress in gradient metasurfaces, JOSA B **33**, A21 (2016).

[71] J. Huang and J. A. Encinar, *Reflectarray Antennas* (Wiley, Piscataway, N.J.–IEEE Press, Hoboken, N.J., 2007), 1st ed.